AIChE

Experimental Investigations of Non-Newtonian/Newtonian Liquid-Liquid Flows in Microchannels

Evangelia Roumpea, Maxime Chinaud, and Panagiota Angeli
Dept. of Chemical Engineering, University College London, Torrington Place, London WC1E 7JE, U.K.

DOI 10.1002/aic.15704
Published online March 27, 2017 in Wiley Online Library (wileyonlinelibrary.com)

The plug flow of a non-Newtonian and a Newtonian liquid was experimentally investigated in a quartz microchannel (200-μm internal diameter). Two aqueous glycerol solutions containing xanthan gum at 1000 and 2000 ppm were the non-Newtonian fluids and 0.0046 Pa s silicone oil was the Newtonian phase forming the dispersed plugs. Two-color particle image velocimetry was used to obtain the hydrodynamic characteristics and the velocity profiles in both phases under different fluid flow rates. The experimental results revealed that the increase in xanthan gum concentration produced longer, bullet-shaped plugs, and increased the thickness of the film surrounding them. From the shear rate and viscosity profiles, it was found that the polymer solution was in the shear-thinning region while the viscosity was higher in the middle of the channel compared to the region close to the wall. Circulation times in the aqueous phase increased with the concentration of xanthan gum. © 2017 The Authors AIChE Journal published by Wiley Periodicals, Inc. on behalf of American Institute of Chemical Engineers *AIChE J*, 63: 3599–3609, 2017
Keywords: non-Newtonian, microchannels, μ-particle image velocimetry

Introduction

Over the last decade, research on microfluidic devices with dimensions in the submillimeter scale has significantly increased driven by process intensification demands. Such systems have found several chemical engineering applications in, among others, mixing, separations, and reactions.[1,2] The small characteristic dimensions and high surface-to-volume ratio in microdevices enhance the role of surface tension over gravitational forces resulting in patterns different to those observed in large-scale flows.[3,4]

Flows of mixtures of two immiscible liquids are very common in chemical processing. The main patterns that have been observed in liquid-liquid microchannel flows are plug, drop, annular, and parallel depending on the competition among interfacial ($\sim\sigma/d$), viscous ($\sim\mu\cdot u/d$), and inertia ($\sim\rho\cdot u\cdot d$) forces.[5] Plug flow, where one phase forms elongated drops (plugs) with size larger than the channel diameter, separated from the channel wall by a thin film, is a common regime which appears for a wide range of flow rates. The internal recirculation within both phases and the presence of the thin film surrounding the plugs enhance mass transfer and make plug flow particularly suitable for liquid-liquid mass-transfer operations and chemical reactions.

Two-phase liquid flows of Newtonian fluids in small channels have been widely studied.[4,6–10] Conversely, even though non-Newtonian fluids are very common industrially, there are very few studies of their flow in microchannels. Non-Newtonian fluids find applications in areas such as enhanced oil recovery, catalytic polymerization reactions, and food processing.[11] From the few studies available, Hunsy and Cooper-White[2] experimentally investigated the formation of microdrops in a T-junction microfluidic device using non-Newtonian aqueous solutions of polyethylene oxide (PEO) as the dispersed phase and organic solutions as the continuous phase. Their results showed that increasing the continuous phase viscosity decreased the drop size whereas the presence of PEO had a negligible effect on the drop size. Fu et al.[12] studied the flow patterns in a T-junction microchannel when aqueous solutions of carboxymethyl cellulose (CMC) were used as the non-Newtonian continuous phase. Using high-speed imaging, they observed four different patterns (slug, droplet, parallel, and jet flow) and found that with increasing polymer concentration, the droplet flow occurred at lower continuous phase superficial velocities. Arratia et al.[13] investigated the filament thinning and breakup of viscoelastic fluids in liquid-liquid flows in a cross-slot microchannel inlet to obtain their extensional viscosity. Chiarello et al.[14,15] studied the formation of oil droplets in shear-thinning, aqueous solutions and introduced an effective Capillary number that took into account the shear-thinning rheology. They observed that the droplet size in the non-Newtonian fluids increased with the flow rate ratio and decreased with increasing continuous phase flow rate.

When polymers are present in one of the phases, it is important to be able to differentiate between the effects of increasing viscosity and of non-Newtonian rheology. For this, it is necessary to have information on the velocity fields and on shear rates. Micro-particle image velocimetry (micro-PIV) has been widely used to obtain the velocity profiles in liquid-liquid microchannel

Correspondence concerning this article should be addressed to P. Angeli, p.angeli@ucl.ac.uk.

Table 1. Properties of the Working Fluids ($T = 20°C$)

Fluid System			ρ (kg/m^3)	μ_C (Pa s) K	μ_C (Pa s) n	σ (mN/m)
Continuous phase	N2	Aqueous glycerol solution (52% wt/wt) + 2000 ppm xanthan gum	1144	0.85	0.36	30.70
	N1	Aqueous glycerol solution (52% wt/wt) + 1000 ppm xanthan gum	1143	0.55	0.39	31.40
	N	Aqueous glycerol solution (52% wt/wt)	1142	0.007		31.80
Dispersed phase	O	Silicone oil	930	0.0046		–

flows.[10,16–20] Kinoshita et al.[21] measured the three-dimensional velocity fields and circulation patterns inside a moving aqueous droplet by confocal microscopy whereas Kashid et al.[16] studied the circulation patterns into plugs during liquid-liquid two-phase flow using PIV. Tsaoulidis and Angeli[22] used an image acquisition system based on bright field PIV to visualize film thickness and recirculation patterns in liquid plugs at small channels of varying size. Chinaud et al.[23] obtained velocity profiles within both liquid phases during plug breakage at the T-junction inlet of a microchannel using a two-color μPIV technique.

In this article, the liquid-liquid plug flow pattern in small channels is investigated when one of the phases is non-Newtonian. Hydrodynamic characteristics such as plug length, shape, and film thickness are studied when shear-thinning xanthan gum solutions at two different concentrations are used as the non-Newtonian continuous phase. In addition, velocity fields in both phases are measured with a two-color micro-PIV system. These are the first studies where velocity profiles are obtained during the two-phase flow of non-Newtonian fluids in small channels and are related to the hydrodynamic characteristics.

Materials and Experimental Setup

For the investigations, two glycerol aqueous solutions containing different concentrations of xanthan gum (Sigma-Aldrich), 1000 (N1) and 2000 ppm (N2), were used as the non-Newtonian phase, while the organic phase was a 0.0046 Pa s silicone oil (from Sigma-Aldrich). Xanthan gum is a polysaccharide biopolymer with a high molecular weight and a wide range of applications in food, pharmaceutical, and oil industries.[24] Glycerol (Sigma-Aldrich) was added in the aqueous phase to match the refractive index of the organic phase and avoid light refraction and optical distortions during the visualization and the PIV studies. It was found that a mixture of 48% wt/wt water and 52% wt/wt glycerol matches the oil refractive index ($n_D^{20} = 1.39$). Measurements were also carried out with the corresponding Newtonian aqueous solution (without xanthan gum) for reference and comparisons.

The physical properties of the fluids are summarized in Table 1. The Advanced Rheometric Expansion System (TA Instruments®) was used to study the rheological behavior of the non-Newtonian solutions. All measurements were carried out at 20°C. The rheometer had a Couette geometry (with bob diameter 16.5 mm, cup size 17 mm, and 0.05 mm gap), and the temperature was controlled with a water bath. The experimental viscosity data of the two xanthan gum solutions are plotted as a function of the shear rate in Figure 1. Both aqueous solutions exhibit a typical shear-thinning behavior with the fluid viscosity decreasing with increasing shear rate. It is noted that the viscosity of the Newtonian solution ($\mu_N = 0.007$ Pa s) is always lower than that of the non-Newtonian ones even at high shear rate values (above 1000 s^{-1} where $\mu_{N1} = 0.014$ Pa s and $\mu_{N2} = 0.016$ Pa s). The power-law model[25] was used to fit the data (see inset in Figure 1)

$$\mu(\dot{\gamma}) = K(\dot{\gamma})^{n-1} \tag{1}$$

where $\mu(\dot{\gamma})$ is the apparent viscosity (Pa s), $\dot{\gamma}$ is the shear rate (s^{-1}), K is the consistency index, and n is the flow behavior index. The values of K and n for the two non-Newtonian solutions are given in Table 1. The interfacial tension, σ, was measured with the Du Noüy ring method (K100 KRUSS GmbH®).

The flow experiments were carried out in a circular microchannel with internal diameter (ID) 200 μm. The microchannel is made of two semicircular channels, etched on quartz chips, that were bonded together thermally (Dolomite® microfluidics). The T-junction inlet is etched in the same quartz chip as the main channel. Using syringe pumps (KDS Scientific®), the two immiscible fluids were introduced separately into the microchannel via a T-junction with branches of the same size as the main channel. Experiments were conducted at different combinations of flow rates of the two phases. The microchannel was initially filled with the aqueous phase, and the oil was introduced subsequently.

In each set of experiments, the aqueous (continuous) phase flow rate was kept constant whereas the organic (dispersed) phase flow rate was increased stepwise. The phase flow rates ranged from 0.01 to 0.1 cm^3/min. Initially, the flow pattern map was obtained using a 3000-Hz high-speed camera (Photron 3000). A white LED backlight with adjustable intensity was used to illuminate the channel. A small amount of commercial, black ink (Pelikan®) was added in the aqueous phase to differentiate between the phases in the captured images. The amount of ink added did not affect the interfacial tension.

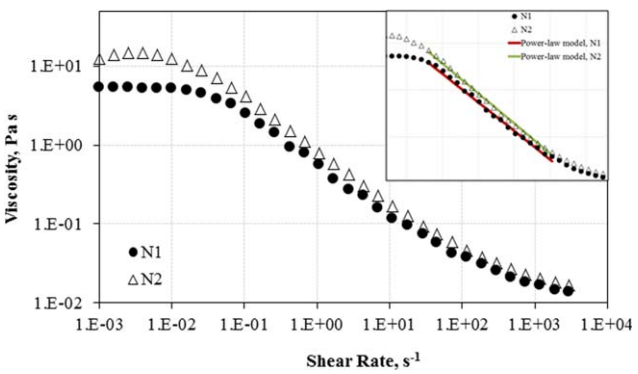

Figure 1. Viscosity vs. shear rate of the non-Newtonian fluids used.

N1 and N2 correspond respectively to the 1000 and 2000 ppm xanthan gum concentration solutions. Inset: Power-law fitting of the viscosity curves. [Color figure can be viewed at wileyonlinelibrary.com]

Table 2. Experimental Conditions Used for Plug Flow

Case	Q_C (cm^3/min)	Q_D (cm^3/min)	$Ca_{(N)}$	$Ca_{(N1)}$	$Ca_{(N2)}$
1	0.06	0.01	0.007	0.012	0.022
2	0.06	0.02	0.008	0.013	0.022
3	0.06	0.03	0.009	0.014	0.024
4	0.07	0.01	0.010	0.014	0.023
5	0.07	0.02	0.011	0.015	0.024
6	0.07	0.03	0.013	0.015	0.025
7	0.08	0.01	0.011	0.014	0.025
8	0.08	0.02	0.012	0.015	0.026
9	0.08	0.03	0.013	0.017	0.027

Images were acquired and processed with image processing software (Photron, High Speed Cameras®). The map indicated the ranges of flow rates where plug flow occurs. Within the plug flow region, further experiments were carried out to measure the plug characteristics and the velocity profiles within the two phases. The conditions for the experiments are summarized in Table 2 together with the corresponding modified Capillary numbers. For the non-Newtonian solutions, the Capillary number was calculated as follows[26]

$$Ca = \mu'_C U_P / \sigma \tag{2}$$

where $\mu'_C = K(\dot{\gamma})^{n-1}$ is the continuous phase viscosity, U_P is the plug velocity, and σ is the interfacial tension. The average shear rate across the channel diameter was calculated as $\dot{\gamma} = \frac{2U_S(1+2n)}{D(1+n)}$ where U_S represents the mean continuous phase velocity, and n the flow behavior index. This definition assumes a power law velocity profile in the channel. Different shear rate definitions have previously been used in the literature depending on whether the fluids have a weak or strong non-Newtonian character.[15,26] The current definition was chosen because of the strong shear-thinning behavior of the xanthan gum solutions investigated here ($n < 0.65$).

The velocity profiles in the two phases during plug flow were studied using a two-color micro-PIV technique.[23] Two types of tracer particles with different fluorescing wavelengths were dispersed, each in one phase. The aqueous phase was seeded with 1-μm carboxylate-modified microspheres FluoSpheres® with orange fluorescent colour (540/560 nm) at a volume ratio of 0.04. In the organic phase, 1-μm blue polystyrene microspheres Fluoro-Max® (350/440 nm) were dispersed at a volume ratio of 0.28 after a drying process. A schematic of the two-color micro-PIV setup is shown in Figure 2. For illumination, a double pulsed Nd:YAG laser (Litron Lasers®) was used that emits a blue (355 nm) and a green (532 nm) wavelength at the same time. The light is guided with an optical fiber to the test section placed at an inverted microscope (Nikon Eclipse Ti-s) with a 10x magnification. The light emitted from the tracer particles is led to a beam splitter (Andor® Technology), which separates the two wavelengths using lenses, a dichroic mirror, and both high and band pass filters. The orange light (560 nm) emitted by the particles in the aqueous phase, is led through the dichroic mirror and a high-pass filter toward a 4 MP, 32 fps CCD camera Link® Base (TSI, Powerview 4 MP) with 2048 × 2048 pixels resolution; the blue light (440 nm) is reflected by the dichroic mirror and is led through the band pass filter to a 12-bit CCD camera Dicam pro® (PCO Sensicam, Dicam pro®) with 1270 × 512 pixels resolution. Both cameras have a 2x magnification lens and are connected to a laser pulse synchronizer (TSI®), which controls the laser pulse delay time and the time between pulses necessary for the flow visualization and the image acquisition. The PIV acquisition frequency is 7 Hz per image pair. The μPIV measurement depth for the blue (355 nm) and green (532) wavelengths is approximately 20 μm (10% of the channel diameter) and 26 μm (13% of the channel diameter), respectively, using an objective lens with magnification M equal to 10x (NA = 0.30, $n = 1$).[27]

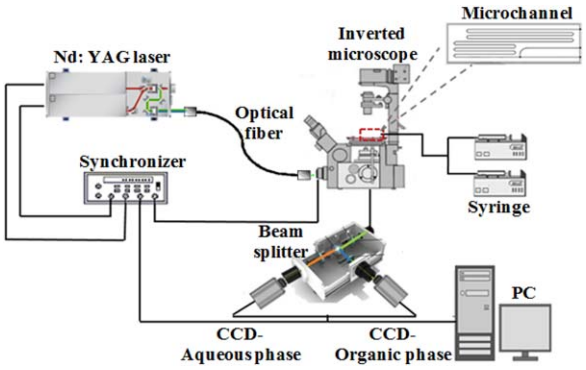

Figure 2. Schematic diagram of the experimental setup and the two-color micro-PIV system.

[Color figure can be viewed at wileyonlinelibrary.com]

The detection of the interface presents a challenge in PIV measurements in two-phase flows, particularly when the refractive indices of the two phases have been matched.[28] To tackle this problem and improve the detection of the aqueous-organic interface, 1 ppm of rhodamine 6G fluorescent dye is also added in the aqueous phase.[29] The fluorescent dye at such small amounts was found to have negligible effects on the fluid properties.

PIV data processing

The acquired PIV images were initially processed using the image processing software Insight 4G, TSI®. For both cameras, the PIV correlation box size was set to 64 × 64 pixels with 50% spatial overlapping which results in a final spatial resolution of 10.56 × 10.56 μm for the aqueous phase and of 24 × 24 μm for the organic phase. A primary-to-secondary correlation peak ratio was used as filter to remove the false vectors whereas vectors outside the seeded phases were set to zero. The effective particle diameter, d_e, is equal to 33.2 μm for the orange fluorescent particles and to 24.1 μm for the blue ones providing an uncertainty equal to $d_e/10M = 0.33$ μm for the aqueous phase and $d_e/10M = 0.24$ μm for the organic phase (where M is the lens magnification).[18,30] The focal plane was located at the center of the channel using the front wall as a reference and maximizing the channel width, giving an additional uncertainty of measured distance of 1.0 μm for the aqueous and 1.5 μm for the organic phase.

The PIV images were treated further with MATLAB R2014a codes developed in house. In the images of the aqueous phase, the interface tracking was based on the rhodamine dye dissolved into the aqueous phase, which resulted in increased background contrast. Based on the intensity histogram of the images, a threshold value was used to binarize the images and reconstruct the interface. The same process was also applied to the organic phase images. However, in this case, the binarization process is based only on the signal of the particles (as there is no dye in the organic phase). The reconstructed contours of both the aqueous and the organic phases

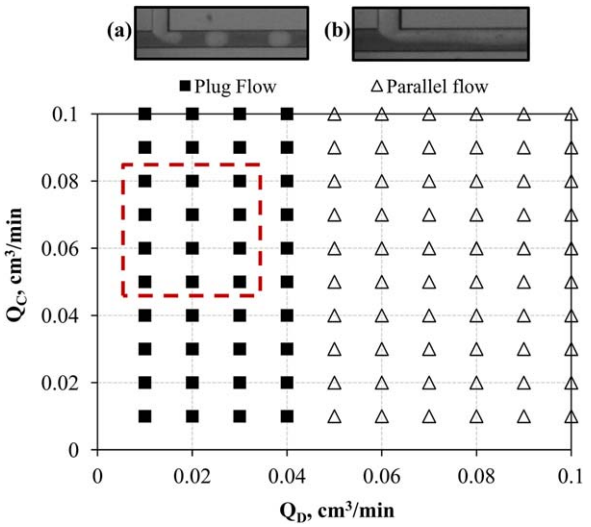

Figure 3. Flow pattern map of the aqueous Newtonian/non-Newtonian 1000 ppm solution and the silicone oil.

The dashed line encloses the area of plug flow when the Newtonian aqueous phase is used. Representative flow patterns (a) plug flow; (b) parallel flow, captured using the high-speed camera. The dark-colored liquid is the aqueous phase whereas the light-colored one is the organic phase. [Color figure can be viewed at wileyonlinelibrary.com]

are subsequently used as an adaptive mask to discriminate the phases and match the velocity fields from each camera. Further to this, a raw image of the microchannel boundaries is acquired and used as the calibration target to match the two recorded signals of the cameras.

During the acquisition process different plugs were recorded which are not necessarily in the same position in the channel. To obtain average velocity fields in each phase, the images obtained from each camera were centered using the tip plug position as reference. For the average velocity fields, 600 micro-PIV images were acquired. However, only 200–300 of the images, depending on the flow rate conditions, corresponded to full-length plugs and were used for the velocity field calculations.

Results and Discussion

Flow pattern map

The flow patterns, which form under different phase flow rates, were studied for the three aqueous solutions. For all conditions studied (i.e., phase flow rates between 0.01 and 0.1 cm^3/min) two different flow patterns were found, namely plug and parallel flow. In plug flow, the *organic 0.0046 Pa s* Newtonian phase always forms the dispersed *plugs* (Figure 3a) irrespective of the side branch of the T-junction used to introduce it in the main channel. In the parallel flow pattern (Figure 3b), the two liquids come in contact at the T-junction and then move in parallel along the channel. The different flow patterns are attributed to the competition among interfacial ($\sim\sigma/d$), inertia ($\sim\rho\cdot u\cdot d$), and viscous forces ($\sim\mu\cdot u/d$). The interfacial forces tend to minimize the interfacial area resulting in plug flow whereas the viscous forces tend to keep the interface smooth. The inertial force extends the interface in the flow direction and dominates in the parallel flow pattern.[31] The different patterns are plotted in Figure 3 for the Newtonian and the 1000 ppm non-Newtonian aqueous phase, in a map with the phase flow rates as coordinates. The patterns for the 2000 ppm non-Newtonian solution are the same as those for the 1000 ppm solution and are not shown here.

As can be seen, for the Newtonian aqueous phase, the plug flow is limited to low dispersed and medium continuous phase flow rates (points inside the dashed square). The range of conditions for plug flow is, however, significantly expanded when the non-Newtonian aqueous solution is used. In particular, plug flow occurred for the whole range of the continuous (aqueous) phase flow rates studied and for an extended range of dispersed (organic) phase flow rates. Plug flow establishes at low dispersed phase flow rates, where the shear forces between the liquids are low. As the dispersed phase flow rate is further increased and the shear force of the continuous phase is not large enough to break the interface into plugs, parallel flow forms (Figure 3). The shift in the boundary between the plug and the parallel flows with the polymer addition could be due to both the change in the shear viscosity and the non-Newtonian rheology of the aqueous continuous phase. Sang et al.,[32] from numerical analysis of droplet formation, found that an increase in Newtonian viscosity delayed the drop break up at the channel inlet and resulted in a decrease in the area of plug flow in the map. However, when power law fluids were used, as the flow behavior index, n, decreased (or the amount of polymer increased), the droplets broke closer to the T-junction and extended the region of plug flow. A similar trend was also found by Fu et al.[12] who investigated the flow patterns of cyclohexane (dispersed phase) and shear-thinning non-Newtonian aqueous solutions (continuous phase) containing different concentrations of CMC. They observed that droplet flow occurred at lower superficial velocity of the continuous non-Newtonian phase with increasing CMC concentration.

Generally, the transition from one pattern to another occurs over a range of flow rates. For the non-Newtonian systems, a transition region was found for all the continuous phase flow rates studied. As the dispersed phase flow rate increased, for constant Q_C, plugs with irregular sizes appeared before parallel flow was established. This transition region occured for Q_D between 0.04 and 0.05 cm^3/min.

The hydrodynamic characteristics of the plug flow were further studied in the main channel using the two-color micro-PIV system for the cases indicated in Table 2.

Plug length

The effect of dispersed phase flow rate, Q_D, on plug size is illustrated in Figure 4 for the Newtonian aqueous solution (N) and $Q_C = 0.07$ cm^3/min. The channel walls are also shown for clarity. From the pictures captured using the two-color PIV (Figures 4a–c), it can be seen that by increasing the dispersed phase flow rate, the plug length increases. A similar trend is also found for both non-Newtonian 1000 ppm (N1) and 2000 ppm (N2) solutions. Plug lengths were averaged over micro-PIV images with a standard deviation for all cases equal to 3.0–15.5%. The results are plotted in Figure 4d where it can be seen that an increase in the polymer concentration produces generally longer oil plugs, that is, $L_{P\,N} < L_{P\,N1} < L_{P\,N2}$, where L_P is the plug length. This difference increases as the dispersed (organic) phase flow rate increases.

An increase in the continuous phase flow rate on the other hand, decreases L_P for the non-Newtonian fluids as can be seen in Figure 5 for dispersed phase flow rate $Q_D = 0.03$ cm^3/min.

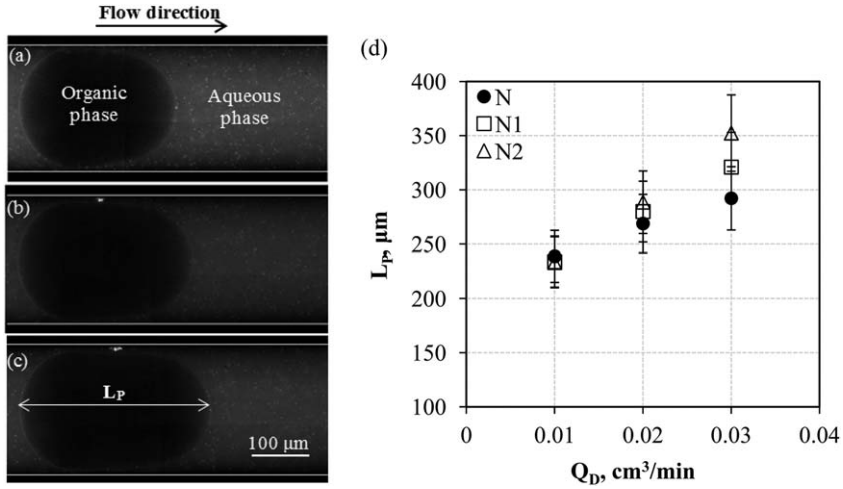

Figure 4. Effect of dispersed phase flow rate on the Newtonian plug size for Q_D (cm^3/min): (a) 0.01, (b) 0.02, (c) 0.03 ($Q_C = 0.07$ cm^3/min), and (d) effect of dispersed phase flow rate on plug length (for constant $Q_C = 0.07$ cm^3/min).

An increase in Q_C from 0.06 to 0.08 cm^3/min reduces the plug length in the N1 and N2 systems by approximately 47 and 55 μm, respectively (15% standard deviation). The trend is similar to this of Hunsy and Cooper-White.[2] Conversely, in the Newtonian system the continuous phase flow rate does not have a significant effect on plug size with a maximum deviation of L_P equal to 17 μm (6% standard deviation). Furthermore, as the xanthan gum concetration increases, longer plugs are produced, for constant phase flow rates.

Chiarello et al.[14] who studied the formation of organic droplets in a T-junction channel using different concentrations of xanthan gum in water, investigated the shear-thinning effect on the droplet size. They compared a xanthan gum/water solution to a glycerol/water (Newtonian) one with similar viscosity and found that the droplet lengths produced in the polymeric mixtures were longer than those obtained in the Newtonian one especially at a high flow rate ratio (under constant continuous phase flow rate). Fu et al.[33] who studied oil drops in shear thinning aqueous solutions with PAAm also found longer plugs in the non-Newtonian solutions compared to the Newtonian ones. The longer plug lengths, however, may not necessarily mean that the plugs have larger volumes. As will be shown later, the film thickness increases when polymers are added in the water phase, and the change in plug length may only be a result of plug elongation. From the PIV images collected, it was found that the plug volumes actually decreased with increasing amount of polymer added in the aqueous phase. Chiarello et al.[15] have also reported this trend with the addition of polymers.

The nondimensional plug lengths are plotted in Figure 6 against the ratio of dispersed to continuous phase flow rates for all conditions studied. As can be seen, the dimensionless plug length increases almost linearly with the flow rate ratio.[14,34–36] Generally, plug lengths in the non-Newtonian systems are larger than in the Newtonian one and increase with the xanthan gum concentration. In addition, at a high flow rate ratio, the increase of plug length with the polymer becomes more significant (see also Figure 4), that is, for $Q_D/Q_C = 0.5$, the L_P of the 2000 ppm solution increases by 32% from the Newtonian case.

The results are also compared with the scaling law for the squeezing regime for plug formation proposed by Garstecki et al.,[34] which is given by

$$\frac{L_P}{D} = 1 + a\frac{Q_D}{Q_C} \tag{3}$$

where D is the internal diameter of the channel, and a is a parameter of the order of one, whose value depends on the

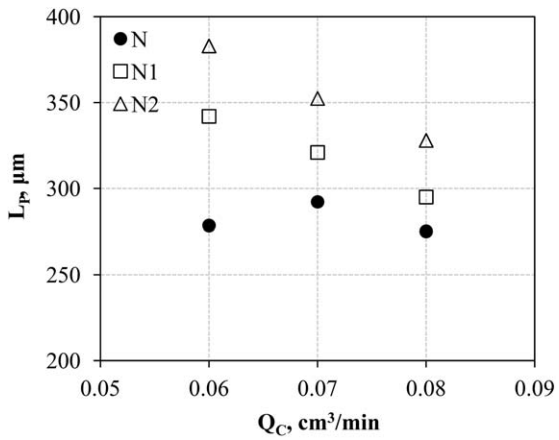

Figure 5. Effect of continuous phase flow rate on plug length L_P (for constant $Q_D = 0.03$ cm^3/min).

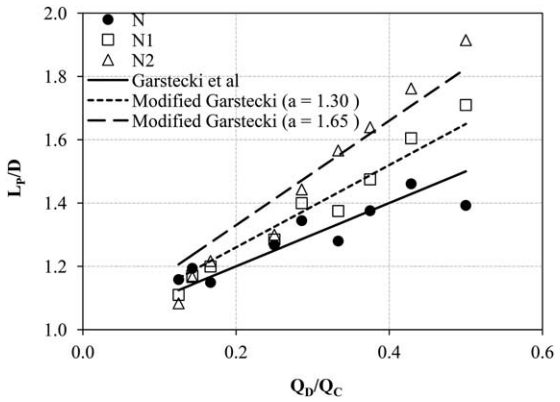

Figure 6. Effect of dispersed to continuous phase flow rate ratio on dimensionless plug length L_p/D.

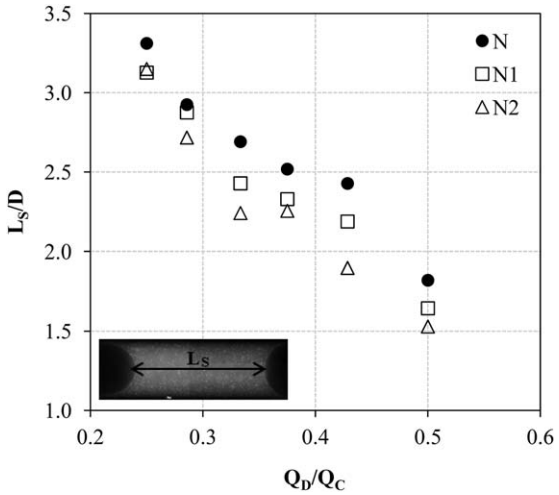

Figure 7. Effect of dispersed to continuous phase flow rate ratio on dimensionless slug length L_S/D.

geometry of the T-junction inlet and of the plug neck during formation. For the Newtonian system, the above model agrees well with the experimental data for $a = 1$ with standard deviation less than 8%. For the non-Newtonian systems, the values of the parameter α that gave the best fit to the experimental data are 1.30 (4.5% maximum error) and 1.65 (10% maximum error) for the 1000 and 2000 ppm xanthan gum solution, respectively. It appears that the addition of polymer does not affect the linear trend and consequently the plug formation mechanism. However, the increase in the slope of the line for different xanthan gum concentrations indicates a geometrical modification of the plug as it forms at the T-junction inlet.

The effect of flow rate ratio on the slug length is shown in Figure 7. As the dispersed phase flow rate increases, the slug length reduces linearly by 45% in all the three aqueous solutions. Furthermore, for constant phase flow rates, increasing the xanthan gum concetration results in slightly shorter slugs (standard deviation for all cases equal to 6.5–13.0%). It should be noted that for $Q_D = 0.01$ cm^3/min where the slug is long, a full-length slug image could not be captured with the current configuration of the PIV system, and no slug length was calculated.

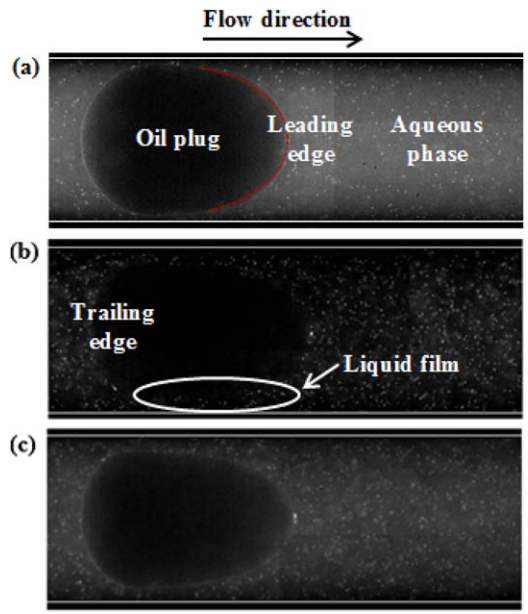

Figure 8. Effect of the polymer addition on plug shape: (a) Newtonian fluid, N, (b) non-Newtonian fluid 1000 ppm, N1, and (c) non-Newtonian fluid 2000 ppm, N2 ($Q_C = 0.07$ cm^3/min and $Q_D = 0.01$ cm^3/min).

[Color figure can be viewed at wileyonlinelibrary.com]

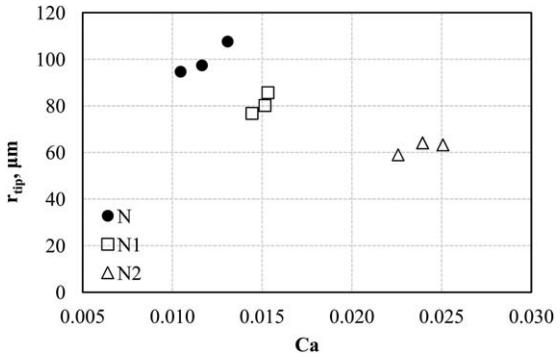

Figure 9. Effect of Capillary number on plug front edge radius for constant $Q_C = 0.07$ cm^3/min and Q_D equal to 0.01, 0.02, and 0.03 cm^3/min.

Plug shape

The rheological properties of the continuous phase are found to affect the curvature of the plug leading edge which is mainly controlled by the balance between interfacial and viscous forces.[37] The plug leading edge was obtained from the μPIV images and is defined as the area from the tip of the plug until the point where the surrounding film has reached a uniform thickness (Figure 8a). As can be seen in Figure 8, the front plug edge curvature increases with increasing polymer concentration in the continuous aqueous phase, and the plug acquires a bullet-shaped profile. In the 2000 ppm polymer concentration system, the decrease in the plug leading edge radius can be as high as 37% compared to the Newtonian case. The radius of the trailing plug edge also decreases (curvature increases) with polymer concentration in the aqueous phase. However, this decrease is less pronounced compared to the front edge and for the case shown in Figure 8 it is about 13%. The same behavior was observed for all the flow rate combinations studied.

The bullet-shaped profile of the leading plug edge has been reported for Taylor bubbles at high Capillary numbers.[38,39] In the present study, high Capillary numbers can be achieved by increasing the continuous phase viscosity or the dispersed phase velocity as the interfacial tension is the same for all the three aqueous solutions. The dependency of the plug front edge radius, r_{tip}, on the Capillary number for the different continuous phases studied is shown in Figure 9 for $Q_C = 0.07$ cm^3/min. The plug radius decreases as the Ca number increases with the polymer addition; this was also seen by Meyer et al.[40] In the non-Newtonian solutions, the viscocity is not homogeneous across the channel. The viscosity is higher in the middle of the channel (see also Figure 15a) where the shear rates are low. As a result, the increased viscous forces in this region overcome the surface tension forces which are not able to sustain the semispherical shape of the plug front, leading to the bullet-shaped profile.

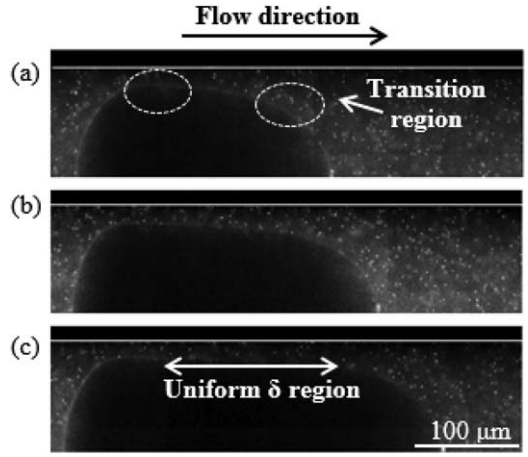

Figure 10. Micro-PIV images highlighting the effect of plug length on film thickness for N2 and Q_D (cm^3/min): (a) 0.01, (b) 0.02, and (c) 0.03 ($Q_C = 0.07$ cm^3/min).

Film thickness

In all cases investigated, the plugs are separated from the channel wall by a thin film of the continuous phase as shown in Figure 8. The film thickness was measured from the images obtained with the micro-PIV system. As can be seen, the film thickness, δ, is not uniform over the entire length of the plug. According to Bretherton,[41] the plug profile can be divided into three different parts: leading edge, trailing edge, and main part. The leading and trailing edge caps join through a transition region with the main part of the plug with uniform film thickness. However, when the plugs are not sufficiently long, a uniform film thickness region may not establish.

Two main plug profiles were observed depending on the plug length. In short plugs, the leading plug edge joins almost immediately the trailing edge, and there is not a region of uniform film thickness (Figures 10a, b). As the plug length increases above $L_P \geq 352$ μm, a region of uniform film thickness can be seen (Figure 10c). This variation in film thickness can pose problems in its measurement. Eain et al.[42] have chosen as measurement location the trailing part of the plug where the film thickness has its lowest value. Other investigators[9,10] have used an average value of the film thickness along the plug, between the leading and trailing edges. This approach

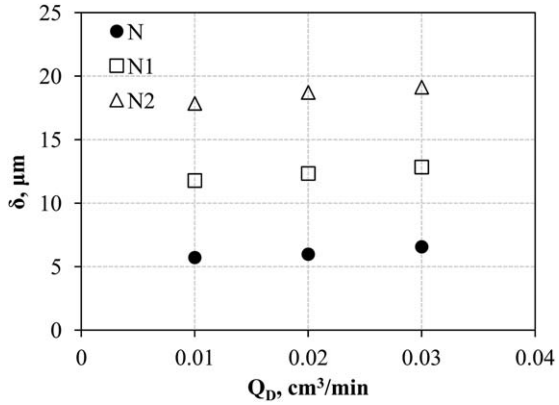

Figure 11. Effect of dispersed phase flow rate on film thickness for different aqueous solutions (for $Q_C = 0.07$ cm^3/min).

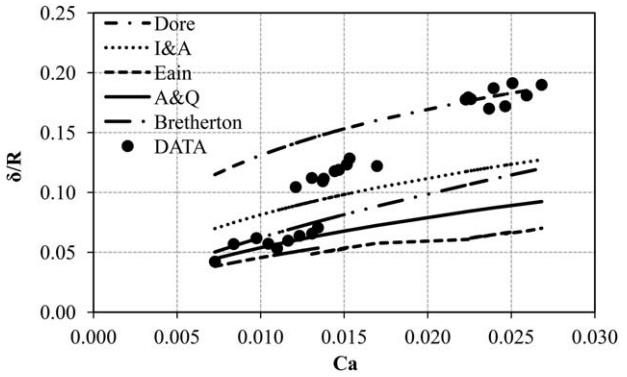

Figure 12. Nondimensional film thickness, δ/R, plotted against the Capillary number for all experimental conditions.

Current results are compared to literature models from Table 3.

was also used here, and an average film thickness was calculated. For low Capillary numbers $Ca \sim 10^{-3}$, where the dimensionless film thickness is $\delta \sim 8$ μm, the standard deviation in the film thickness measurements could be as high as 20%. At high Capillary numbers, which correspond to the non-Newtonian solutions, the standard deviation in the film thickness measurements is below 10% for all the cases studied.

The effect on film thickness of the continuous phase flow rate and rheology can be seen in Figure 11. With increasing amount of xanthan gum in the aqueous phase and front plug edge curvature, the film thickness increases. At the Newtonian system, the liquid film corresponds to approximately 3% of the channel diameter, whereas at the 2000 ppm xanthan gum (N2) system the film thickness is almost 10% of the channel diameter. Additionally, for a constant continuous phase flow rate, $Q_C = 0.07$ cm^3/min, the film thickness increases with increasing dispersed phase flow rate. As reported in the literature, in Newtonian systems, the film thickness is increased either by increasing the velocity or the viscosity of the continuous phase, which leads to increased Ca number.[22,42] However, for these Newtonian cases, the maximum increase of the film thickness is by a factor of 2 (even at higher Ca number, i.e., $0.003 < Ca < 0.180$) while for the shear-thinning fluids used in the experiments, the increase is by a factor of 4 ($0.007 < Ca < 0.027$).

The experimental nondimensional film thickness results, δ/R, for all conditions studied, are plotted in Figure 12 against the Capillary number $Ca = \mu'_c \cdot U_P/\sigma$, which for the non-Newtonian systems was calculated from Eq. 2. From the different velocities that have been used in the literature for the calculation of the Capillary number (e.g., plug, slug, or continuous phase velocities[4,22,43]), the plug velocity was chosen because it is related to the film thickness (see Bretherton[41]; Eain et al.[42]). The dimensionless film thickness was found to increase with increasing Capillary number. The results are also compared against the predictions of commonly used models given in Table 3. Many of the literature correlations for film thickness, shown in Figure 12, are developments of the theoretical analysis by Bretherton[41] who found that the film thickness in gas-liquid Taylor flow was proportional to $Ca^{2/3}$. The data for the Newtonian system agreed well with the model by Aussillous and Quéré,[47] with an average error of 7%, who modified Bretherton's correlation to fit the experimental data

Table 3. Experimental Studies of Liquid Film Thickness in Two-Phase Flow (Bandara et al.[44])

Authors	Model	Flow Condition
Bretherton[41]	$1.34\ Ca^{2/3}$	$10^{-4} \le Ca \le 10^{-2}$
Suo and Griffith[45]	$\left(1-\sqrt{\frac{U_{TPM}}{U_B}}\right)$	$Re \ll 1$
Irandoust and Anderson[46]	$0.36\left[1-\exp\left(-3.08\ Ca^{0.54}\right)\right]$	$9.5 \times 10^{-4} < Ca < 1.9$ $0.42 < Re < 860$
Aussillous and Quéré[47]	$\frac{1.34\ Ca^{2/3}}{1+3.35\ Ca^{2/3}}$	$10^{-3} \le Ca \le 1.4$
Han and Shikazono[43]	$\frac{1.34\ Ca^{2/3}}{1+3.13Ca^{2/3}+0.504\ Ca^{0.672}\ Re^{0.589}-0.352We^{0.629}})$	$Ca < 0.3$ and $Re < 2000$
Dore et al.[10]	$0.30\left[1-\exp\left(-6.90\ Ca^{0.54}\right)\right]$	$0.007 < Ca < 0.159$
Eain et al.[42]	$0.35Ca^{0.354}We^{0.097}$	$0.002 < Ca < 0.119$ $14.46 < Re < 100.96$

by Taylor.[48] At $Ca < 0.015$, the results also agreed well with the model by Bretherton[41] with an average error of 9%. These models however, did not predict well the experimental results for the non-Newtonian systems (average error > 54%). Irandoust and Anderson[46] proposed an empirical correlation for film thickness in gas-liquid Taylor flow, which predicted the present results in both Newtonian and non-Newtonian systems with an average error of 33%. The model by Dore et al.[10] predicted reasonably well the experimental data for the non-Newtonian system (11% average error) but not for the Newtonian ones, with an average error of about 56%. The model by Eain et al.[42] which included the effects of inertial forces via the Weber number, did not predict the non-Newtonian data well with an average error of 90% whereas for the Newtonian mixtures, the average error was 24%.

Circulation patterns in the plugs and the slugs

Representative average velocity fields in both the organic and the aqueous phases, obtained with the two-color μPIV system, are shown in Figure 13. The horizontal component of the velocity is dominant at the main flow direction along the x axis. The velocity is maximum at the core of both the plug and the slug and decreases toward the channel walls and the liquid/liquid interface.

The horizontal velocity profiles at the middle of the plug and slug, (dotted rectangle in Figure 13) for two extreme cases (Newtonian, N and 2000 ppm xanthan gum, N2) are compared in Figures 14a and b, respectively, for $Q_C = 0.07$ cm^3/min and $Q_D = 0.03$ cm^3/min. Within the plug, the velocities are slightly larger for the non-Newtonian system compared to the Newtonian one (Figure 14b). This is expected since the addition of the polymer resulted in a bullet-shaped plug and increased film thickness, which led to a higher plug velocity. As can be seen in Figure 14a, the velocity profile in the slug changes shape with the addition of the polymer. For the Newtonian system, fully developed laminar flow is expected in the middle of the slug, and this is reflected in the parabolic profile. However, in the non-Newtonian system the profile is flat in the

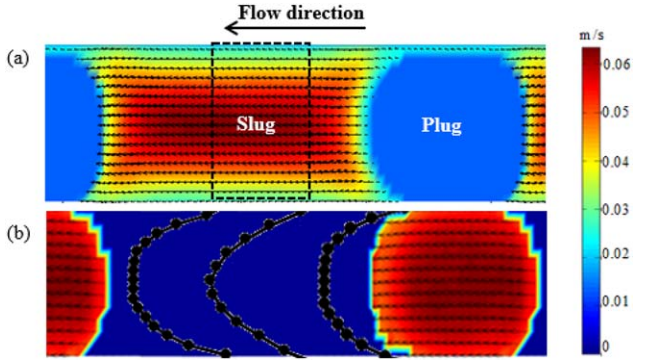

Figure 13. Averaged total velocity fields in (a) slug and (b) plug for Newtonian fluid N and flow rates $Q_C = 0.07$ cm^3/min and $Q_D = 0.03$ cm^3/min.

Dotted rectangle indicates the fully developed laminar flow area. [Color figure can be viewed at wileyonlinelibrary.com]

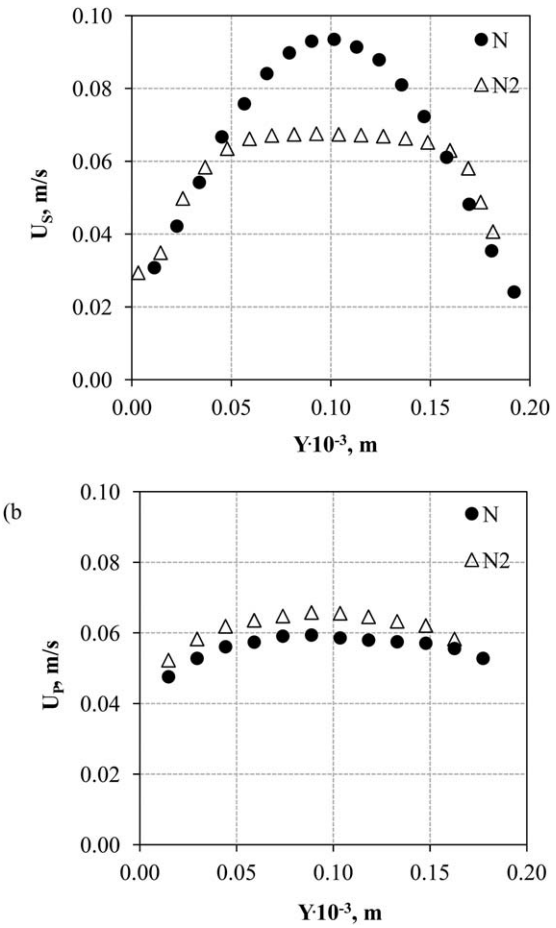

Figure 14. Average velocity profiles of the horizontal component of the velocity in the middle of (a) the slug and (b) the plug for different concentrations of xanthan gum ($Q_C = 0.07$ cm^3/min and $Q_D = 0.03$ cm^3/min).

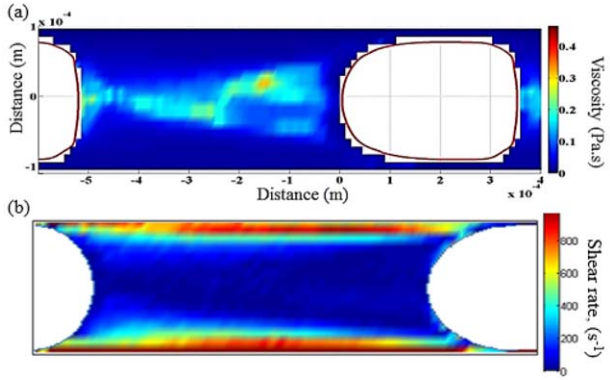

Figure 15. (a) Viscosity profile and (b) shear rate profile in the aqueous non-Newtonian 2000 ppm slug ($Q_C = 0.07$ cm^3/min and $Q_D = 0.03$ cm^3/min).

[Color figure can be viewed at wileyonlinelibrary.com]

middle, which is characteristic of the laminar velocity profile of a power law fluid.

The nonhomogeneous viscosity and shear rate profiles in the slug were also calculated based on the PIV velocity profiles and are presented in Figure 15 for the 2000 ppm non-Newtonian solution. As can be seen, the shear rate varies from 1000 s^{-1} (close to channel wall) to almost zero (in the middle area of the channel) resulting in an increase in the viscosity of the xanthan gum solutions by one order of magnitude, that is, from 0.02 Pa s in the wall (1000 s^{-1}) to 0.2 Pa s in the middle (0–3 s^{-1}). These values correspond to the shear-thinning region of the solution (see Figure 1). Figure 15 clearly shows that the hydrodynamic characteristics of the plugs formed in shear-thinning xanthan solutions are a result of both shear-thinning behavior and increased viscosity.

The change in the velocity profiles, particularly in the slug, when polymer is added is expected to affect the circulation patterns. The recirculation patterns in the slug were calculated by subtracting the slug velocity from the averaged local velocity field and are shown in Figure 16 for a continuous phase flow rate $Q_C = 0.07$ cm^3/min and dispersed phase flow rate $Q_D = 0.03$ cm^3/min. As shown in Figure 16a, for the Newtonian aqueous phase a clear recirculation pattern forms which consists of two distinct vortices, counter rotating, and symmetrical about the channel axis. The recirculation pattern is also symmetric with respect to the centerline of the slug and extends along the whole slug length. Two stagnation zones are visible, and the backflow of the particles is pronounced. When the 2000 ppm xanthan gum solution is used as continuous phase, the two stagnation zones move toward the channel wall, while they remain symmetric about the channel axis (Figure 16b) resulting in a less intense recirculation pattern.

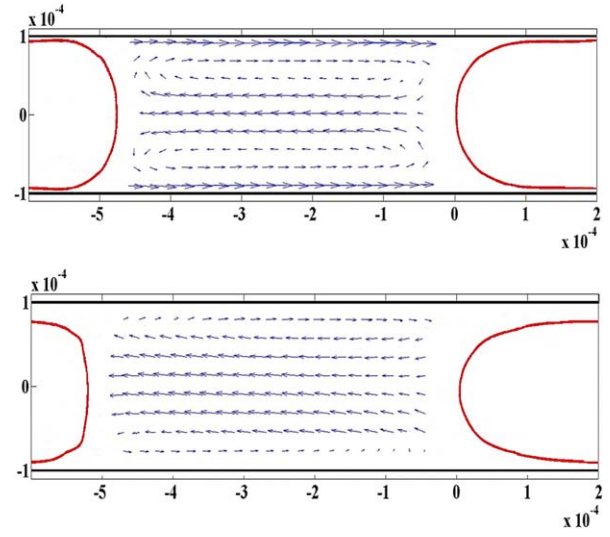

Figure 16. Effect of xanthan gum concentration on circulation patterns in aqueous slugs for (a) Newtonian fluid, N and (b) non-Newtonian 2000 ppm fluid, N2 ($Q_C = 0.07$ cm^3/min and $Q_D = 0.03$ cm^3/min).

[Color figure can be viewed at wileyonlinelibrary.com]

The circulation within the slugs can be quantified with the dimensionless circulation time, τ.[49] This is defined as the time taken by the liquid to move from one end of the slug to the other, T_L, over the slug travel time, T_S (time needed for the slug to travel a distance equal to its own length; $T_S = L_S/U_S$ where L_S is the slug length and U_S is the slug velocity)

$$\tau \equiv \frac{T_L}{T_s} = \frac{T_L U_S}{L_S} \tag{4}$$

The dimensionless circulation time can be calculated from the current velocity profiles obtained from PIV on a plane in the middle of the slug as follows[10]

$$\tau_{cir} = \frac{L_S y_0}{\int_0^{y_0} u(x,y)dy} \frac{U_S}{L_S} = \frac{U_S y_0}{\Delta y \sum_{i=1}^{i=N} v_i} \tag{5}$$

where y_o is the location of the stagnation point projected onto the observation plane.

The dimensionless circulation time from Eq. 5 is plotted against the slug length in Figure 17. As can be seen, the circulation time is almost uniform in the main part of the slug body indicating that the circulation patterns are regular and increases close to the front and back interfaces. When the xanthan gum solution is used, the circulation time increases slightly under the same flow rate conditions. The average dimensionless circulation time corresponding to the plateau of the curve is equal to 4.76 and 5.44 for the Newtonian and non-Newtonian systems, respectively. Similar trends were

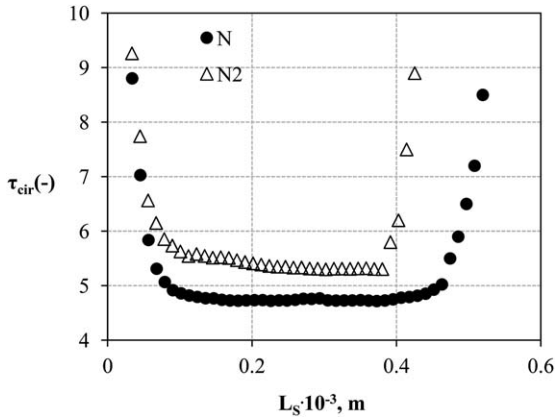

Figure 17. Effect of xanthan gum concentration on the dimensionless circulation time in the slug for flow rates $Q_C = 0.07$ cm^3/min and $Q_D = 0.03$ cm^3/min.

Table 4. Dimensionless Circulation Times in the Continuous Aqueous Slug Phase for All Cases Studied

Experimental Conditions		Dimensionless Circulation Time		
Q_C (cm^3/min)	Q_D (cm^3/min)	N	N1	N2
0.06	0.01	–	–	–
	0.02	2.95	3.83	4.35
	0.03	3.28	4.38	4.57
0.07	0.01	–	–	–
	0.02	4.01	4.41	4.95
	0.03	4.76	5.02	5.44
0.08	0.01	–	–	–
	0.02	5.17	5.75	6.31
	0.03	6.49	6.91	7.23

found for all the flow rates studied as can be seen in Table 4. As was mentioned before when $Q_D = 0.01$ cm^3/min, a full-length slug image could not be captured with the current PIV system, and no circulation patterns could be calculated for these cases.

Conclusions

The hydrodynamic characteristics of the plug flow of a non-Newtonian and a Newtonian liquid in a microchannel were investigated using a two-color micro-PIV system. Two glycerol aqueous solutions containing different concentrations of a shear-thinning polymer, xanthan gum (1000 and 2000 ppm) were used as the non-Newtonian phase while silicone oil was the Newtonian one forming the dispersed plugs under all conditions. It was found that the addition of xanthan gum extended the area of plug flow to higher superficial phase velocities compared to the Newtonian case. Plug lengths increased when polymer was added, while in all cases their size increased when the dispersed to continuous phase flow rate ratio increased. The front plug edge curvature increased with polymer concentration, and the plug acquired a bullet-shaped profile. The thickness of the aqueous film between the plug and the channel wall increased with increasing concentration of the polymer in the continuous phase; it also increased with the dispersed phase velocity. Using a modified Capillary number to account for the non-Newtonian continuous phase viscosity, the suggested models were not able to predict both Newtonian and non-Newtonian film thickness data satisfactorily. Good agreement was found between the non-Newtonian data and the film thickness models by Irandoust and Anderson[46] and Dore et al.[10] for $0.012 < Ca < 0.027$.

The velocity profiles obtained from the PIV measurements showed that the addition of xanthan gum resulted in a higher plug velocity. Within the non-Newtonian slug, the velocity profiles were found to be flat in the middle of the channel as expected for a power law fluid. Higher viscosities were also found in this region compared to the region close to the channel wall. The addition of the polymer also changed the circulation patterns in the aqueous continuous phase. Compared to the Newtonian cases, in the non-Newtonian slugs the stagnation points moved toward the channel wall while the dimensionless circulation times increased, indicating a less intense mixing.

Future studies will investigate the process of plug formation at the channel inlet and link it to the plug and slug sizes observed in the main channel. Different types of non-Newtonian fluids will be used to understand the effect of rheology on the flow properties of the two-phase mixtures.

Acknowledgments

This project was funded by the UK Engineering and Physical Sciences Research Council (EPSRC) Programme Grant MEMPHIS. The authors would like to acknowledge the EPSRC Instrument Pool for the loan of the high-speed camera.

Literature Cited

1. Angeli P, Gavriilidis A. Hydrodynamics of Taylor flow in small channels: a review. *Proc Inst Mech Eng C J Mech.* 2008;222(5):737–751.
2. Hunsy J, Cooper-White J. The effect of elasticity on drop creation in T-shaped microchannels. *J Non-Newtonian Fluid Mech.* 2006;137:121–136.
3. Gupta A, Kumar R. Effect of geometry on droplet formation in the squeezing regime in a microfluidic T-junction. *Microfluid Nanofluidics.* 2010;8:799–812.
4. Dessimoz A, Cavin L, Renken A, Kiwi-Minsker L. Liquid-liquid two-phase flow patterns and mass transfer characteristics in rectangular glass microreactors. *J Chem Eng Sci.* 2008;63:4035–4044.
5. Su Y, Chen G, Yuan Q. Effect of viscosity on the hydrodynamics of liquid processes in microchannels. *Chem Eng Technol.* 2013;37:427–434.
6. Kashid M, Agar D. Hydrodynamics of liquid-liquid slug flow capillary microreactor: flow regimes, slug size and pressure drop. *Chem Eng J.* 2007;131:1–13.
7. Salim A, Fourar M, Pironon J, Sausse J. Oil–water two-phase flow in microchannels: flow patterns and pressure drop measurements. *Can J Chem Eng.* 2008;86:978–988.
8. Su Y, Zhao Y, Chen G, Yuan Q. Liquid-liquid two-phase flow and mass transfer characteristics in packed microchannels. *J Chem Eng Sci.* 2010;65:3947–3956.
9. Jovanovic J, Zhou W, Rebrov EV, Nijhuis TA, Hessel V, Schouten JC. Liquid-liquid slug flow: hydrodynamics and pressure drop. *J Chem Eng Sci.* 2011;66:42–54.
10. Dore V, Tsaoulidis D, Angeli P. Mixing patterns in water plugs during water/ionic liquid segmented flow in microchannels. *J Chem Eng Sci.* 2012;80:334–341.
11. Tsakiroglou C. Correlation of the two-phase flow coefficients of porous media with the rheology of shear-thinning fluids. *J Non-Newtonian Fluid Mech.* 2004;177:1–23.
12. Fu T, Wei L, Zhu C, Ma Y. Flow patterns of liquid-liquid two-phase flow in non-Newtonian fluids in rectangular microchannels. *Chem Eng Process Process Intensif.* 2015;91:114–120.
13. Arratia PE, Gollub JP, Durian DJ. Polymeric filament thinning and breakup in microchannels. *Phys Rev E.* 2008;77(3):1–6.
14. Chiarello E, Derzsi L, Pierno M, Mistura G, Piccin E. Generation of oil droplets in a non-Newtonian liquid using a microfluidic T-junction. *Micromachines.* 2015;6:1825–1835.
15. Chiarello E, Gupta A, Mistura G, Pierno M, Sbragaglia M. Droplet breakup driven by shear thinning solutions in a microfluidic T-junction. *Soft Condens Matter.* 2016. Available from https://arxiv.org/abs/1610.07800.
16. Kashid M, Gerlach I, Goetz S, Franzke J, Acker J, Platte F, Agar D, Turek S. Internal circulation within the liquid slugs of a liquid-liquid slug-flow capillary microreactor. *Ind Eng Chem.* 2005;44:5003–5010.
17. Wang C, Nguyen N, Wong T. Optical measurement of flow field and concentration field inside a moving nanoliter droplet. *Sens Actuators A Phys.* 2007;133:317–322.
18. Silva G, Leal N, Semiao V. Mirco-PIV and CFD characterization of flows in a microchannel: velocity profiles, surface roughness and Poiseuille numbers. *Int J Heat Fluid Flow.* 2008;29(4):1211–1220.
19. Sathe M, Thaker I, Strand T, Joshi J. Advanced PIV/LIF and shadowgraphy system to visualize flow structure in two-phase bubbly flows. *Chem Eng Sci.* 2010;65:2431–2442.
20. Fang W, Ting S, Hsu CW, Chen Y, Yang J. Locally enhanced concentration and detection of oligonucleotides in a plug-based microfluidic device. *Lab Chip.* 2012;12:923–931.
21. Kinoshita H, Kaneda S, Fujii T, Oshima M. Three-dimensional measurement and visualization of internal flow of a moving droplet using confocal micro-PIV. *Lab Chip.* 2007;7:338–346.
22. Tsaoulidis D, Angeli P. Effect of channel size on liquid-liquid plug flow in small channels. *AIChE J.* 2016;62:315–324.

23. Chinaud M, Roumpea E, Angeli P. Studies of plug formation in microchannel liquid–liquid flows using advanced particle image velocimetry techniques. *Exp Therm Fluid Sci*. 2015;69:99–110.
24. Ghannam M, Abu-Jdayil B, Esmail N. Experimental investigation of crude oil–xanthan emulsions flow behavior. *J Pet Sci Res*. 2014; 3(1):1–15.
25. Harris J. *Rheology and Non-Newtonian Flow*. New York: Longam Inc., 1977.
26. Lindner A, Bonn D, Meunier J. Viscous fingering in a shear-thinning fluid. *Phys Fluids*. 2000;12(2):256–261.
27. Meinhart C, Wereley S, Gray M. Volume illumination for two-dimensional particle image velocimetry. *Meas Sci Technol*. 2000;11: 809–814.
28. Khodaparast S, Borhani N, Thome J. Application of micro particle shadow velocimetry μPSV to two-phase flows in microchannels. *Int J Multiphase Flow*. 2014;62:123–133.
29. Mohamed-Kassim Z, Longmire E. Drop coalescence through a liquid/liquid interface. *Phys Fluids*. 2004;16(7):2170–2181.
30. King C, Walsh E, Grimes R. PIV measurements of flow within plugs in a microchannel. *Microfluid Nanofluidics*. 2007;3:463–472.
31. Foroughi H, Kawaji M. Viscous oil–water flows in a microchannel initially saturated with oil: flow patterns and pressure drop characteristics. *Int J Multiphase Flow*. 2011;37(9):1147–1155.
32. Sang L, Hong Y, Wang F. Investigation of viscosity effect on droplet formation in T-shaped microchannels by numerical and analytical methods. *Microfluid Nanofluidics*. 2009;6(5):621–635.
33. Fu T, Ma Y, Li H. Breakup dynamics of slender droplet formation in shear-thinning fluids in flow-focusing devices. *Chem Eng Sci*. 2016;144:75–86.
34. Garstecki P, Fuerstman M, Stone H, Whitesides G. Formation of droplets and bubbles in a microfluidic T-junction-scaling and mechanism of break-up. *Lab Chip*. 2006;6(3):437–446.
35. Mansour M, Kawahara A, Sadatomi M. Experimental investigation of gas-non-Newtonian liquid two-phase flows from T-junction mixer in rectangular microchannel. *Int J Multiphase Flow*. 2015;72:263–274.
36. Christopher G, Noharuddin N, Taylor J, Anna S. Experimental observations of the squeezing-to-dripping transition in T-shaped microfluidic junctions. *Phys Rev E*. 2008;78(3):036317.
37. Zhao Y, Chen G, Yuan Q. Liquid-liquid two-phase flow patterns in a rectangular microchannel. *AIChE J*. 2006;52:4052–4060.
38. Kashid M, Renken A, Kiwi-Minsker L. Gas–liquid and liquid–liquid mass transfer in microstructured reactors. *Chem Eng Sci*. 2011;66: 3876–3897.
39. Liu H, Vandu C, Krishna R. Hydrodynamics of Taylor flow in vertical capillaries: flow regimes, bubble rise velocity, liquid slug length, and pressure drop. *Ind Eng Chem Res*. 2005;44(14):4884–4897.
40. Meyer C, Hoffmann M, Schluter M. Micro-PIV analysis of gas-liquid Taylor flow in a vertical oriented square shaped fluidic channel. *Int J Multiphase Flow*. 2014;67:140–148.
41. Bretherton F. The motion of long bubbles in tubes. *J Fluid Mech*. 1961;10(2):166–188.
42. Eain M, Egan V, Punch J. Film thickness measurements in liquid-liquid slug flow regimes. *Int J Heat Fluid Flow*. 2013;44:515–523.
43. Han Y, Shikazono N. Measurement of the liquid film thickness in micro tube slug flow. *Int J Heat Fluid Flow*. 2009;30(5):842–853.
44. Bandara T, Nguyen N, Rosengarten G. Slug flow heat transfer without phase change in microchannels: a review. *Chem Eng Sci*. 2015; 126:283–295.
45. Suo M, Griffith P. Two phase in capillary tubes. *J Basic Eng*. 1964; 86:576–582.
46. Irandoust S, Anderson B. Liquid film in Taylor flow through a capillary. *Ind Eng Chem Res*. 1989;28(11):1684–1688.
47. Aussillous P, Quéré D. Quick deposition of a fluid on the wall of a tube. *Phys Fluids*. 2000;12:2367–2371.
48. Taylor G. Deposition of a viscous fluid on the wall of a tube. *J Fluid Mech*. 1961;10(2):161–165.
49. Thulasidas T, Abraham M, Cerro R. Flow patterns in liquid slugs during bubble-train flow inside capillaries. *Chem Eng Sci*. 1997; 52(17):2947–2962.

Manuscript received Nov. 8, 2016, and revision received Feb. 5, 2017.